Technical Advance **Ophthalmology**

Graphical abstract

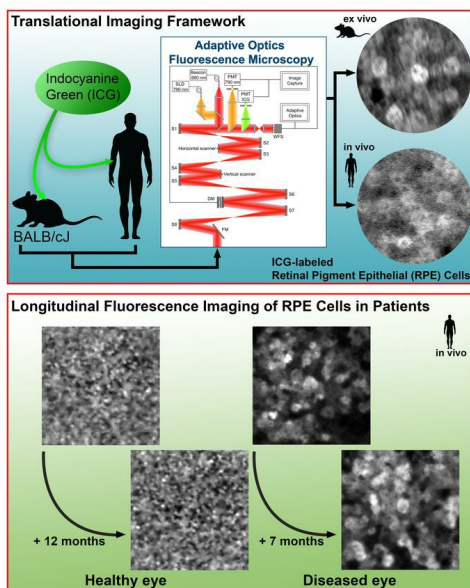# Longitudinal adaptive optics fluorescence microscopy reveals cellular mosaicism in patients

HaeWon Jung,[1] Jianfei Liu,[1] Tao Liu,[1] Aman George,[1] Margery G. Smelkinson,[2] Sarah Cohen,[3] Ruchi Sharma,[1] Owen Schwartz,[2] Arvydas Maminishkis,[1] Kapil Bharti,[1] Catherine Cukras,[1] Laryssa A. Huryn,[1] Brian P. Brooks,[1] Robert Fariss,[1] and Johnny Tam[1]

[1]National Eye Institute, NIH, Bethesda, Maryland, USA. [2]National Institute of Allergy and Infectious Disease, Research Technologies Branch, NIH, Bethesda, Maryland, USA. [3]University of North Carolina – Chapel Hill, Chapel Hill, North Carolina, USA.

The heterogeneity of individual cells in a tissue has been well characterized, largely using ex vivo approaches that do not permit longitudinal assessments of the same tissue over long periods of time. We demonstrate a potentially novel application of adaptive optics fluorescence microscopy to visualize and track the in situ mosaicism of retinal pigment epithelial (RPE) cells directly in the human eye. After a short, dynamic period during which RPE cells take up i.v.-administered indocyanine green (ICG) dye, we observed a remarkably stable heterogeneity in the fluorescent pattern that gradually disappeared over a period of days. This pattern could be robustly reproduced with a new injection and follow-up imaging in the same eye out to at least 12 months, which enabled longitudinal tracking of RPE cells. Investigation of ICG uptake in primary human RPE cells and in a mouse model of ICG uptake alongside human imaging corroborated our findings that the observed mosaicism is an intrinsic property of the RPE tissue. We demonstrate a potentially novel application of fluorescence microscopy to detect subclinical changes to the RPE, a technical advance that has direct implications for improving our understanding of diseases such as oculocutaneous albinism, late-onset retinal degeneration, and Bietti crystalline dystrophy.

Introduction

Recent improvements in imaging, proteomics, genomics, and data science have enabled the rigorous analysis of the heterogeneity of tissues at the single cell level (1, 2). However, characterization of this natural biological variation has been largely limited to cultured cells or to ex vivo approaches that do not permit longitudinal assessment of living cells directly in the living organism. Understanding and characterizing in vivo mosaicism has important implications for revealing the onset and progression of disease at the cellular level. In this paper, we present an all-optical technique to evaluate the long-term stability of mosaicism in the living human eye based on the combination of adaptive optics (AO) with indocyanine green (ICG) ophthalmoscopy to image the retinal pigment epithelial (RPE) mosaic (3).

RPE cells form a monolayer in the outer retina, where they play an important role in maintaining the visual cycle and photoreceptor health (4). From a population level (i.e., considering cells at the tissue level), they exhibit relative uniformity in topology and size, albeit with some variation in density and spacing dependent on the retinal eccentricity (5). However, despite this uniform appearance, there are variations in melanin and lipofuscin pigment content and distribution (6), which become even more pronounced at the single cell level (7). The remarkable cell-to-cell mosaicism of the RPE monolayer also manifests with striking differences in gene and protein expression, as well as susceptibility to oxidative damage (7). Understanding this innate diversity could give important insights into how and why ocular diseases involving the RPE, such as Best vitelliform macular dystrophy (8, 9), Bietti crystalline dystrophy (BCD) (10, 11), Leber congenital amaurosis (12, 13), late-onset retinal degeneration (L-ORD) (14–16), or age-related macular degeneration (17) preferentially affect some RPE cells of the eye and not others. Visualization of RPE cells directly in patients' eyes is also an important first step toward unraveling relationships between RPE cells and photoreceptors in health and disease (18).

RPE cells have been very challenging to image in the clinical setting due to the presence of mela-nosomes that are packed with light-absorbing melanin pigment. Techniques such as optical coherence tomography and fundus autofluorescence, which indirectly provides information about melanin and lipo-fuscin (19, 20), have provided a means to evaluate the overall status of the RPE tissue. However, at the point that these techniques provide information, dramatic cellular changes have already occurred. One limitation has been that it is difficult to resolve individual cells without a method to compensate for the optical imperfections of the eye. To that end, AO (21) combined with autofluorescence has led to direct visualization of individual RPE cells (5, 22). Taking advantage of alternate intrinsic and extrinsic sources of contrast, there is now a growing list of AO-based techniques for imaging RPE cells (3, 5, 22–26), all of which have had limited demonstrated success in imaging diseased eyes. In this paper, we will expand upon our previously developed AO-ICG technique (3) that is based on the uptake of a U.S. Food and Drug Administration–approved (FDA-approved), extrinsic fluorophore from the vasculature into the RPE and present results from our custom-designed AO-ICG instrumentation that we have continued to refine. We investigated the short- and long-term stability of the heterogeneous AO-ICG RPE signal in healthy individuals and show that this mosaicism is an inherent property of the in vivo RPE mosaic that has clin-ical utility for visualizing and quantifying disruptions of the RPE mosaic and for tracking the stability or degree of change to the RPE during developmental and degenerative diseases.

Results

Robustness of heterogeneous AO-ICG RPE pattern enables quantification of cell spacing in the living human eye. A characteristic AO-ICG fluorescence pattern was observed in every healthy eye that we imaged, and we used it to create, to our knowledge, the largest in vivo database to date of human foveal RPE cell-to-cell spacing (Figure 1A and Supplemental Figure 1; supplemental material available online with this article; https://doi.org/10.1172/jci.insight.124904DS1). The observed pattern in this larger cohort was consistent with our earlier findings in a smaller cohort of 3 healthy subjects (3). In the fovea, each RPE cell appears to contain the same level of fluorescence across the entire cell, leading to the possibility of identifying individual cells based on the assumptions that neighboring cells contain different levels of uniform fluorescence and that cells within a small region of interest (ROI) are relatively uniform in size. Based on these assumptions, we leveraged a superpixel segmentation algorithm (27) to automatically outline possible cell borders and assist with subsequent cell identification, which was done manually by correcting the centroids of automated identifications (Figure 1B). Using this semiautomated approach, the average foveal RPE cell-to-cell spacing (Figure 1C) was found to be 14.3 ± 1.0 μm (23 eyes from 14 healthy subjects: subject 1 (S1) to S14, age 34.7 ± 9.5 years; mean ± SD, range 21–52; for subjects with multiple visits, data from the first visit was used; see Supplemental Table 1). These values are consistent with published values, including our previous report quantifying foveal RPE cell-to-cell spacing using AO near-infrared autofluorescence (AO-IRAF) (14.0 ± 1.4 μm, 8 eyes from 8 healthy subjects, age 27.2 ± 7.0 years, range 21–40) (5). For the 9 subjects with both eyes imaged, RPE spacing measurements between contralateral eyes was consistent, although additional data is needed to further characterize the similari-ties and differences across contralateral eyes ($P < 0.05$, one-way ANOVA) (Figure 1D). The distribution of ICG fluorescence calculated from the automated segmentation results varied across subjects (Supplemen-tal Figure 2). The combined distribution of ICG fluorescence across all RPE cells from all eyes ($n = 1,399$) was unimodal and well approximated by the Weibull distribution (Figure 1E). These distributions suggest that the range of ICG dye fluorescence varies continuously across a range (as opposed to being a binary hyper- vs. hypofluorescent event). Based on our observation that this heterogeneous signal was robust and present in every eye imaged, across a range of ages and races (Supplemental Table 1), we surmise that the intriguing pattern that we observe is a physiologically normal intrinsic property of the healthy RPE tissue.

Improved resolution enables in vivo visualization of RPE nuclei and cone photoreceptor inner segments at eccen-tric locations. Although we collected the large majority of our AO-ICG data in the fovea for this study, we found that eccentric RPE cells also exhibited a similar pattern (Supplemental Figure 3), further supporting the notion that the heterogeneous AO-ICG signal observed is a property of the RPE tissue as a whole. The distribution of ICG fluorescence in 1,974 automatically segmented eccentric RPE cells was also unimodal (Supplemental Figure 3, K and L). Despite the presence of what appeared to be hypofluorescent nuclei (Supplemental Figure 3), there was no significant difference in the distributions of fluorescence compar-ing eccentric to foveal RPE cells ($n = 1,399$ foveal cells, 1,974 eccentric cells, $P = 0.06$, Kruskal-Wallis
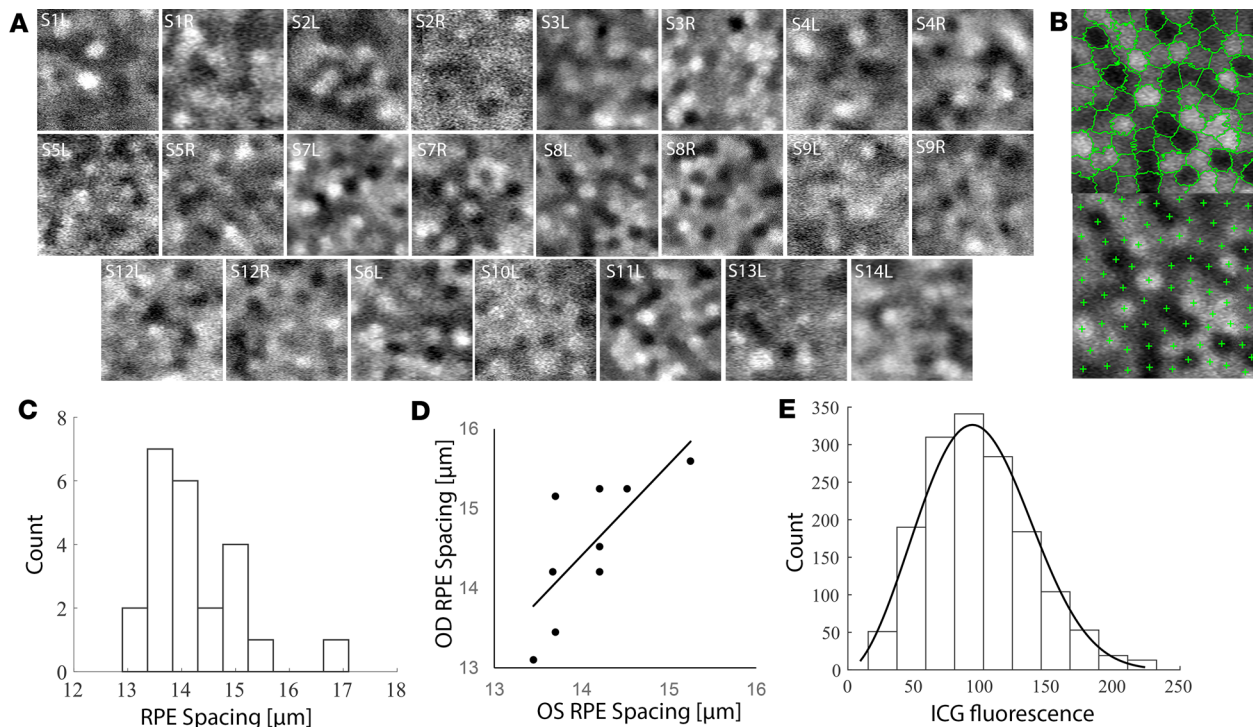
Figure 1. Fluorescence pattern observed in all healthy eyes. Example adaptive optics enhanced indocyanine green (AO-ICG) images of retinal pigment epithelial (RPE) cells acquired from the living human eye. All regions of interest (ROIs) are 100 μm × 100 μm. (**A**) Foveal RPE cells. Subject codes are indicated (Supplemental Table 1) (L, left eye; R, right eye). (**B**) Foveal RPE cell-to-cell spacing (average distance between centers of neighboring RPE cells). Top, approximate outlines of homogeneous-intensity regions generated by superpixel segmentation (27); bottom, centroids of automatically segmented regions were manually corrected. (**C**) Histogram of RPE spacing across all eyes. (**D**) RPE spacing in left eye (OS) vs. right eye (OD) for 9 subjects ($P <$ 0.05, one-way ANOVA). (**E**) Histogram of ICG fluorescence intensity across all 1,399 RPE cells from **A**. Solid line, fit to Weibull distribution.

one-way ANOVA). Our initial report of eccentric AO-ICG images showed that there was an imprinting effect from overlying cone photoreceptors (3), likely due to the optical fiber properties of cones (28) that appear to pattern or locally condense the excitation light (29), which we confirmed to be the case for S11, left eye (S11L). However, in subject S10L, using simultaneously captured, coregistered split detection images of cone photoreceptor inner segments alongside AO-ICG, we demonstrate that the RPE nuclei (hypofluorescent centers) are not artifacts of this imprinting (Supplemental Figure 3, A–J). Coregistration of these images is not significantly affected by chromatic aberrations since the same light source is used for split detection and ICG fluorescence detection channels. The observation that ICG can be used to visualize RPE nuclei under certain circumstances is further corroborated by images from subsequent sections in this manuscript. It is also consistent with our earlier histological results in mice showing that systemically delivered ICG accumulates in the cytoplasmic space, leaving nuclei visible as hypofluorescent areas (3). Quantification of the average number of cones per RPE cell across the eccentricities of 4.0–5.0 mm revealed a cone/RPE ratio of 1.44 ± 0.51 (mean ± SD, $n = 25$ RPE cells), which was within the expected range for healthy subjects (approximately 1.30 ± 0.20) (5). This shows that our multimodal AO imaging approach enables new possibilities for unraveling neuron-epithelial interactions in the living human eye.

Dynamic evolution and subsequent persistence of ICG fluorescence pattern in RPE cells following systemic administration. There is a dynamic evolution of the AO-ICG signal that begins with the passage of dye through the choroidal vasculature, during which RPE cells take up the dye (30). Registration of sequentially acquired AO-ICG videos based on simultaneously captured scattered light imaging channels (Supplemental Video 1) reveals that, in some subjects, the heterogeneous AO-ICG RPE signal reaches stability at approximately 5 minutes after i.v. injection (Figure 2) (see time to stability [TTS] in Supplemental Table 1). Interestingly, during the initial 5 minutes, we observe changing levels of intracellular fluorescence with hyperfluorescent cells appearing hypofluorescent over time, and vice versa, with these changes occurring even in adjacent cells. These findings suggest that the late-phase ICG signal represents a stable equilibrium of fluorescence levels that is reached for each cell (black outline; S7, right eye [S7R]; Figure 2A). In tracking the fluorescence

and change in fluorescence of individual RPE cells across time, the most rapid changes can be seen to occur in the initial 2 minutes after injection (Figure 2B). Although there are still some changes in the relative fluorescence of individual cells after 5 minutes (Figure 2B), the overall pattern at 6 minutes after injection compared with several hours after injection is nearly indistinguishable, which is consistent with our previous findings (3). In all subjects (Figure 1), the pattern remains clearly visible for hours after injection.

Follow-up imaging performed several days following injection in 3 eyes from 2 subjects revealed that the heterogeneous AO-ICG signal was still present, albeit much weaker (Figure 2C), consistent with an early report that showed that detectable levels of ICG dye persists in the eye beyond 24 hours following injection (31). Baseline imaging performed before injection confirmed that there was no ICG signal present in any eyes, aside from the much weaker AO-IRAF signal.

Topology of the choriocapillaris influences but does not determine the formation of the heterogeneous AO-ICG signal in the RPE. To explore the possibility that RPE cells directly overlying blood vessels were more likely to contain more ICG dye than those not above vessels, we imaged the choriocapillaris using AO-ICG in human eyes (in vivo) and compared these images to coregistered images of the overlying heterogeneous AO-ICG RPE pattern (Supplemental Figure 4 and Supplemental Table 2). We categorized RPE cells into 2 categories based on segmentation of choriocapillaris image regions into vessels and flow voids. Quantitative comparison of the ICG fluorescence in RPE cells above vessels compared with above flow voids revealed that the late-phase AO-ICG fluorescence intensity of RPE cells above flow voids was slightly higher than the late-phase AO-ICG fluorescence intensity of RPE cells above choriocapillaris vessel segments ($P < 0.05$, 2-tailed paired t test) (Supplemental Figure 4 and Supplemental Table 2), which is exactly opposite of the expectation that RPE cells overlying vessel segments would contain more ICG than those above flow voids.

Translational imaging framework reveals that the AO-ICG heterogeneity arises independently of melanin in RPE cells. RPE cells contain melanosomes that are packed with melanin pigment granules, which absorb near-infrared light (32). ICG is particularly prone to quenching effects (33) due to its small Stokes shift. Given that the light levels used for imaging in the human eye (μW) are an order of magnitude lower than those typically used in microscopy (mW) due to light-safety limits (34), and that there can be strikingly different amounts of melanin pigment present in neighboring RPE cells (7), it follows that the AO-ICG pattern could be affected by heterogeneous quenching of either excitation light or emitted fluorescence. In this section, we introduce a translational imaging framework — using murine RPE cells ex vivo, primary human RPE cells in culture, and human cells in vivo — to establish that the observed AO-ICG pattern is not wholly the result of a heterogeneous melanin distribution in RPE cells.

First, we utilized RPE flatmounts from albino mice to establish that the heterogeneous ICG pattern can arise in the absence of melanin. We previously demonstrated that we could induce ICG uptake into RPE cells with systemic injection of ICG in mice to parallel i.v. administration in humans (3). We applied this same approach of ICG administration in albino mice. Images of excised unfixed albino RPE flatmounts using the same light source and detectors that were used for human AO-ICG imaging (see Methods) revealed a heterogeneous AO-ICG RPE pattern (Figure 3, A–D), which was similar to what was observed in normally pigmented human subjects (Figure 1).

Next, we used a combination of ex vivo and in vivo approaches to explore whether the heterogeneous pattern was a result of quenching by melanin. Melanin pigment in RPE cells can be visualized ex vivo alongside fluorescent microscopy (Figure 3E). Following incubation with ICG, primary human RPE cells take up ICG dye in the cytoplasmic space, leaving an area of hypofluorescence in the nuclei — which does not take up ICG dye, as we reported earlier (Supplemental Figure 3). The fluorescence of ICG rises above that of the background IRAF melanin (Figure 3, E–H). Direct comparison of pigmentation levels with ICG fluorescence reveals a subtle reduction of ICG fluorescence in some areas with heavy pigmentation (solid boxes, Figure 3, E and F). However, in areas with similar pigmentation (dotted boxes, Figure 3, E and F), variation in ICG fluorescence persists, suggesting that melanin is not the sole driver of the variation in fluorescence levels.

Although transmitted light microscopy can readily visualize melanin pigment granules ex vivo, it cannot be applied to the living human eye in the same manner. Instead, it is possible to optimize imaging to detect the much weaker IRAF signal, which colocalizes with melanin (Figure 3, I–K) and can be used as a proxy. There is a small difference in depth of field between the transmitted light and IRAF detection channels, which causes some minor differences in the composite image (Figure 3K); however, close examination of a z-stack acquired in the same cells confirms that there is excellent colocalization between melanosomes and the IRAF signal (Supplemental Video 2). Based on this colocalization between melanin and IRAF, we compared AO-IRAF
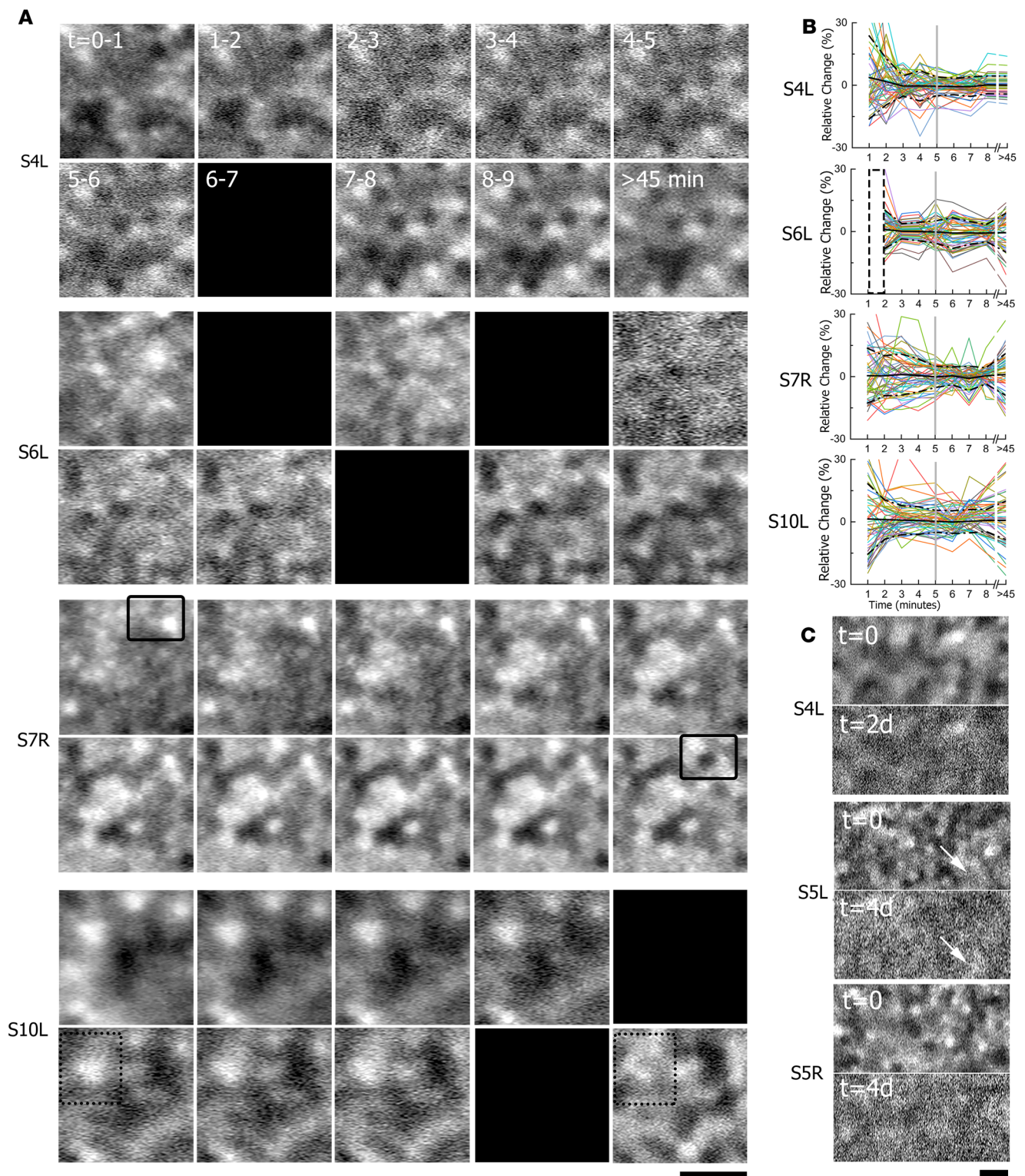
Figure 2. Dynamic establishment of heterogeneous pattern. The same retinal regions imaged at different time points, corrected for eye motion, registered together, and normalized for intensity (based on histogram stretching) following indocyanine green (ICG) dye administration, in human subjects. (**A**) The AO-ICG exhibits spatial dynamics until about 5 minutes, after which the heterogeneous pattern stabilizes. Black subpanels indicate missing data sequences (i.e., not acquired or unusable data). In S7R, the solid black outline represents some cells starting bright and ending dim; others start dim and end bright. In S10L, the dotted outline represents that, although the large majority of cells reached stability after about 5 minutes, there was 1 region that showed a diminished fluorescence after 45 minutes. (**B**) Relative AO-ICG fluorescence change (%) measured in cells over time. Intensities at each time point were normalized to the average fluorescence intensity of the ROI, and then the percent change in intensity from 1 time point relative to the previous time point was calculated. In the case of missing data denoted by black boxes in (**A**), data is plotted as the

average of neighboring values, except for S6L, where it was not possible to reliably calculate the time change for the first minute (dotted box) . Gray vertical bar indicates 5 minute time point at which the heterogeneous pattern is established. The mean and 1 SD are shown in black solid and dotted lines, respectively. The increase in variance at the t > 45 minute time point is likely due to a weaker SNR, which would lead to a greater degree of intensity normalization (histogram stretching). (**C**) The AO-ICG signal persists for days following injection (*n* = 3 eyes) but gets progressively weaker and is barely visible after 4 days. Scale bars: 50 μm.

images of foveal RPE cells in the living human eye to coregistered AO-ICG images of the same RPE cells (images acquired before and after ICG administration). Following segmentation of RPE cells, direct comparison of AO-IRAF (Figure 3, L and N) and AO-ICG (Figure 3, M and O) fluorescence values revealed no apparent relationship between the 2 (Figure 3, P and Q) (S10L [*P* = 0.21, *n* = 324 cells], S14L [*P* = 0.26, *n* = 425 cells], one-way ANOVA). It should also be noted that there are neighboring RPE cells with similar levels of fluorescence in the early stage of ICG uptake into RPE cells (imaged in healthy pigmented human subjects) (Figure 2A), which makes the observed heterogeneity unlikely to be the result of quenching since the melanin content of individual cells is unlikely to change on this timescale of several minutes). Taken together, these results suggest that the heterogeneous pattern is not an artifact of melanin content.

Repeatability of AO-ICG pattern reveals long-term mosaicism of the RPE. Not only does the heterogeneous AO-ICG RPE pattern show stability over a period of days after initial injection, but a new injection 3–12 months afterward elicits a remarkably similar overall pattern of fluorescence intensity (Figure 4 and Supplemental Figure 5) in 10 eyes from 5 healthy subjects. Baseline imaging prior to injection of ICG dye for both visits confirmed that there was no detectable ICG dye present in the RPE prior to injection. To quantify changes in fluorescence across visits, we used an automated algorithm developed for longitudinal AO-ICG data (27) and found that 97.6% ± 1.5% of the pattern remained stable over time (mean ± SD, 10 eyes, 5 pairs of 500 μm × 500 μm ROIs per eye). There was no difference observed in the amount of the pattern that remained stable between visits spaced 3–4 months (6 eyes, 97.6% ± 1.4%) compared with 12 months apart (4 eyes, 97.6% ± 1.9%), suggesting that the mosaicism observed is conserved for long periods of time (well beyond 12 months).

Clinical applications of AO fluorescence microscopy reveals subclinical progressive RPE changes. The long-term repeatability of the mosaicism observed using AO-ICG provides a unique opportunity to track the RPE over time in the clinic. Here, we demonstrate that, with further improvements in instrumentation, translation of this technique previously demonstrated in healthy subjects (whose eyes are generally more amenable to obtaining high-quality images) to patients with retinal disease (whose eyes are significantly more challenging to image) is possible. The overall success rate of imaging the RPE using AO-ICG was 100% for healthy eyes (*n* = 23 eyes), which — as far as we are aware — is much higher than that of most other AO-based techniques for imaging the RPE, indicating a high potential for successful imaging in diseased eyes. We applied our technique to evaluate the status of RPE cells in oculocutaneous albinism (OCA) and 2 different inherited retinal degenerations: L-ORD, and BCD (Figure 5 and Figure 6, Supplemental Table 3).

OCA is an autosomal recessive condition characterized by reduced melanin pigment in the RPE and foveal hypoplasia. Although the photoreceptor packing reaches normal ranges (35), the state of the RPE remains unclear. We were able to obtain successful images in 3 of 4 patients with OCA. All patients had mild to moderate nystagmus, which poses challenges for the current state of AO instruments (Figure 5). Despite the reduction in ocular pigmentation (Figure 5, A–C), AO-ICG images of foveal RPE cells (Figure 5, D–F) were qualitatively similar to those of normally pigmented human subjects, supporting the notion that heterogeneities in melanin and AO-ICG arise independently of each other. This in vivo human data was also corroborated by the fact that the overall pattern was similar across those of African and non-African descent (Figure 1 and Supplemental Table 1) and was also consistent with our results from mice and cell imaging data. In 2 patients with OCA, AO-ICG images at eccentric locations also showed the characteristic AO-ICG heterogeneity (Figure 5, G–J), consistent with our previous findings in a healthy eye (Supplemental Figure 3; eccentric imaging was unsuccessful in the other patients due to nystagmus). The combined AO-ICG fluorescence intensity distribution of 2 patients with OCA (Figure 5K) was similar to that of pigmented subjects (*P* = 0.34, *n* = 5,182 RPE cells, Kruskal-Wallis one-way ANOVA). We excluded patient P4 from the intensity analysis due to the low signal to noise of the images. Quantification of foveal RPE spacing in the patients revealed that spacing was significantly larger than normal ranges, indicating a possible role for RPE cells in OCA (P1, 19.3 μm; P3, 19.6 μm; P4, 21.5 μm; *P* < 0.01, 2-tailed *t* test).

Live murine RPE tissue (*ex vivo*)
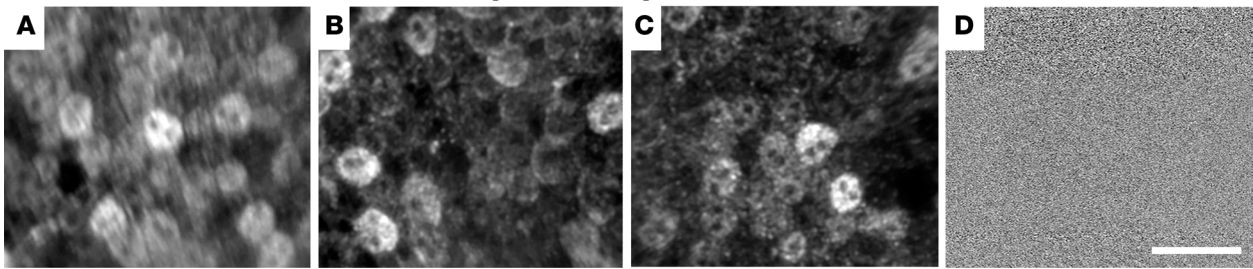
Live human RPE cells (*ex vivo*)
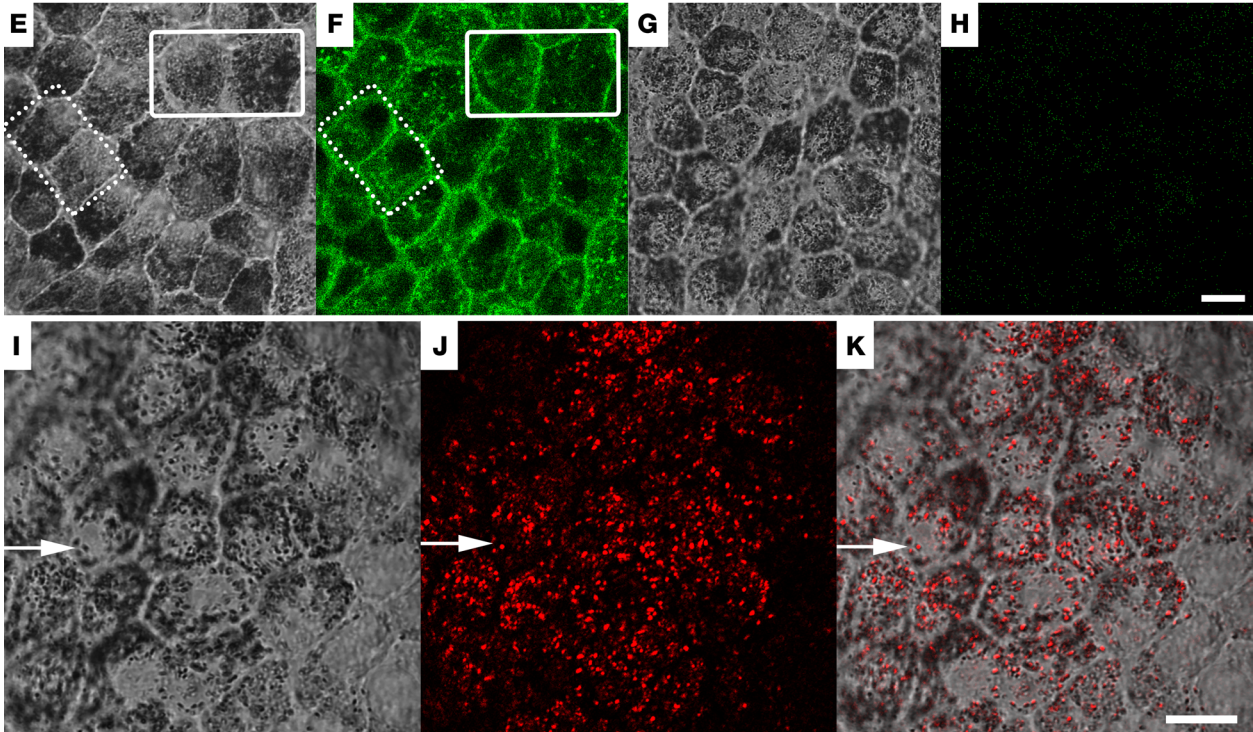
Human RPE cells (*in vivo*)
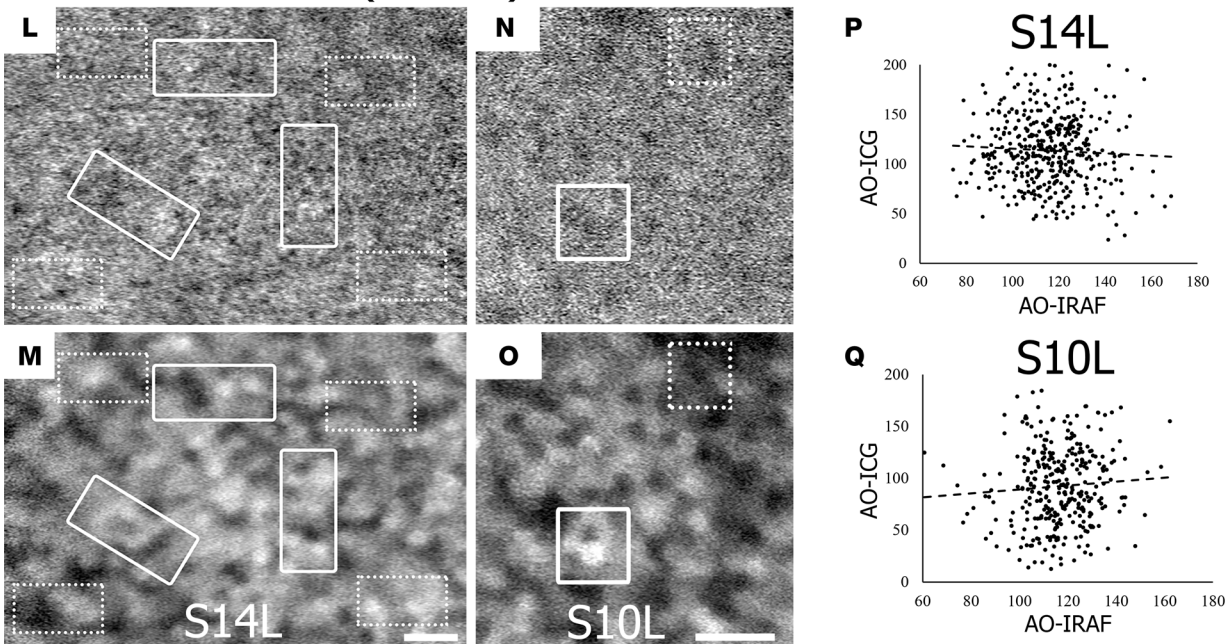
Figure 3. Imaging RPE cell ICG uptake across cultured cells, mice, and humans. Translational imaging framework to evaluate the effects of melanin pigment on ICG signal as assessed by custom confocal microscopes outfitted with near-infrared excitation and emission capabilities. (**A–D**) AO-ICG images of unfixed, fresh RPE flatmounts from (**A–C**) 3 BALB/cJ mice that were systemically injected with ICG and (**D**) 1 BALB/c mouse that was not injected with ICG. The heterogeneous pattern was observed with ICG accumulating in the cytoplasmic space, revealing the binuclear murine RPE cells. Images in **A–D** are histogram adjusted between the minimum and maximum intensity values of each image. (**E–H**) Transmitted light (**E** and **G**) and ICG fluorescence (**F** and **H**) collected from live fetal RPE cells grown in culture. The heterogeneous melanin distribution can be seen (dark areas) in the transmitted light images. ICG-incubated RPE cells (**F**) exhibit substantially higher fluorescence than control RPE cells that have not been incubated with ICG (**H**). Images in **F** and **H** were acquired using the same imaging parameters. Comparison of areas of heavy vs. light pigmentation reveals a subtle quenching of the ICG fluorescence signal in some areas (solid boxes) but not others (dotted boxes). There is a faint infrared autofluorescence (IRAF) visible in **H** that can be enhanced by increasing the laser power. (**I–K**) Induced pluripotent stem cell–derived RPE cells from a pigmented human donor grown in culture imaged using transmitted light (**I**) and IRAF (**J**). Individual melanin granules visible in **I** colocalize with areas of IRAF as can be seen in **K** (white arrows). A z-stack through these cells is shown in Supplemental Video 2. (**L** and **N**) Adaptive optics enhanced infrared autofluorescence (AO-IRAF) image of foveal RPE cells in the living human eye prior to ICG injection. (**M** and **O**) AO-ICG image of coregistered RPE cells following ICG injection. Comparison of areas of brighter and darker IRAF reveals a subtle quenching of the AO-ICG in some areas (solid boxes) but not others (dotted boxes). (**P** and **Q**) There was no relationship between AO-IRAF and AO-ICG fluorescence in individual cells (S10L, $P = 0.21$, $n = 324$ cells; S14L, $P = 0.26$, $n = 425$ cells; one-way ANOVA). Dotted lines, univariate linear regression. Scale bars: (**A–D**) 50 μm, (**E–K**) 10 μm, (**L** and **M**) 100 μm, (**N** and **O**) 50 μm.

Next, we investigated the AO-ICG signal in a patient with L-ORD, a rare, autosomal dominant condition caused by mutations in the *C1QTNF5* gene, expressed in the RPE, and resulting in loss of central vision by the seventh decade of life (14, 15). Patients are typically asymptomatic until the fifth decade of life. Early clinical findings of the disease include subretinal drusenoid deposits (accumulations occurring at the apical side of the RPE) followed by sub-RPE accumulations, which ultimately progress to frank atrophy but initially spare the fovea (16). Using AO-ICG, we evaluated the status of foveal RPE cells in a patient in the early stages of the disease (age, 55 years; Figure 6, D–F). The heterogeneous pattern of the foveal RPE cells was similar to those of healthy eyes (Figure 6, A–C) with a stable heterogeneous pattern across a time period of 12 months (98.7% stability, which was within the limits of our normative data; z-score, 0.76). Foveal RPE spacing was also within normal limits (14.2 μm for both visits in a coregistered ROI; z-score, –0.1). There was 1 small area of hypofluorescence that developed in the second visit that may indicate subtle changes at the single cell level (arrows, Figure 6, E and F). Interestingly, despite qualitatively similar histograms (Figure 6J), the distribution of fluorescence intensity was significantly different compared with our normative data from the fovea ($P < 0.001$, $n = 128$ RPE cells, Kruskal-Wallis one-way ANOVA). It is unclear whether the difference in distribution is clinically meaningful. Overall, these findings demonstrate normal RPE imaging findings at the fovea at the early stages of disease, which is consistent with ancillary clinical studies.

In the patient with BCD, we observed dramatic differences in the RPE size and fluorescence distribution. BCD is a rare, autosomal recessive condition caused by mutations in the *CYP4V2* gene, characterized by crystalline deposits in the retina and cornea (10, 11). Patients are noted to have a progressive retinal degeneration that is thought to affect the RPE. Using AO-ICG, we show that the RPE cells are affected in a patient with BCD (Figure 6, G–I). Although we found long-term preservation of AO-ICG mosaicism across all healthy subjects imaged, in this patient with BCD, longitudinal AO-ICG images showed dramatic changes across 2 visits over a time span of 7 months (84.5% stability across 2 visits; z-score, –8.7) (Figure 6, H and I). In the fovea, quantification of RPE cells in this patient revealed significantly enlarged RPE cells when compared with our AO-ICG normative data (100 μm × 100 μm ROI near the fovea; average RPE spacing across 2 visits in the patient was 24.3 μm, which is a 1.7-fold increase compared with normal values from this manuscript; z-score, 10), which is consistent with a recent report using an induced pluripotent stem cell (iPSC) model of BCD showing enlarged RPE cells (36). Across the foveal region, it appears that RPE cell size is highly variable in this patient with BCD, in contrast to the uniformly sized foveal RPE cells observed across all healthy subjects. In larger RPE cells, RPE nuclei can be seen (arrows, Figure 6, H and I), consistent with the other data reported in this paper. These RPE nuclei further corroborate our claim that there is substantial enlargement in RPE cell size in this patient.

There was a change in the distribution of fluorescence of cells in this patient (Figure 6K), and the overall distribution of fluorescence intensities was significantly different compared with normal ($P < 0.001$, Kruskal-Wallis one-way ANOVA). The degree of change in RPE cells at the fovea was not apparent when assessed using conventional clinical imaging techniques for evaluating the RPE, including fundus autofluorescence and optical coherence tomography; however, the change was readily apparent when visualized using ICG, illustrating the potential utility of this approach. RPE spacing in the patient, mea-
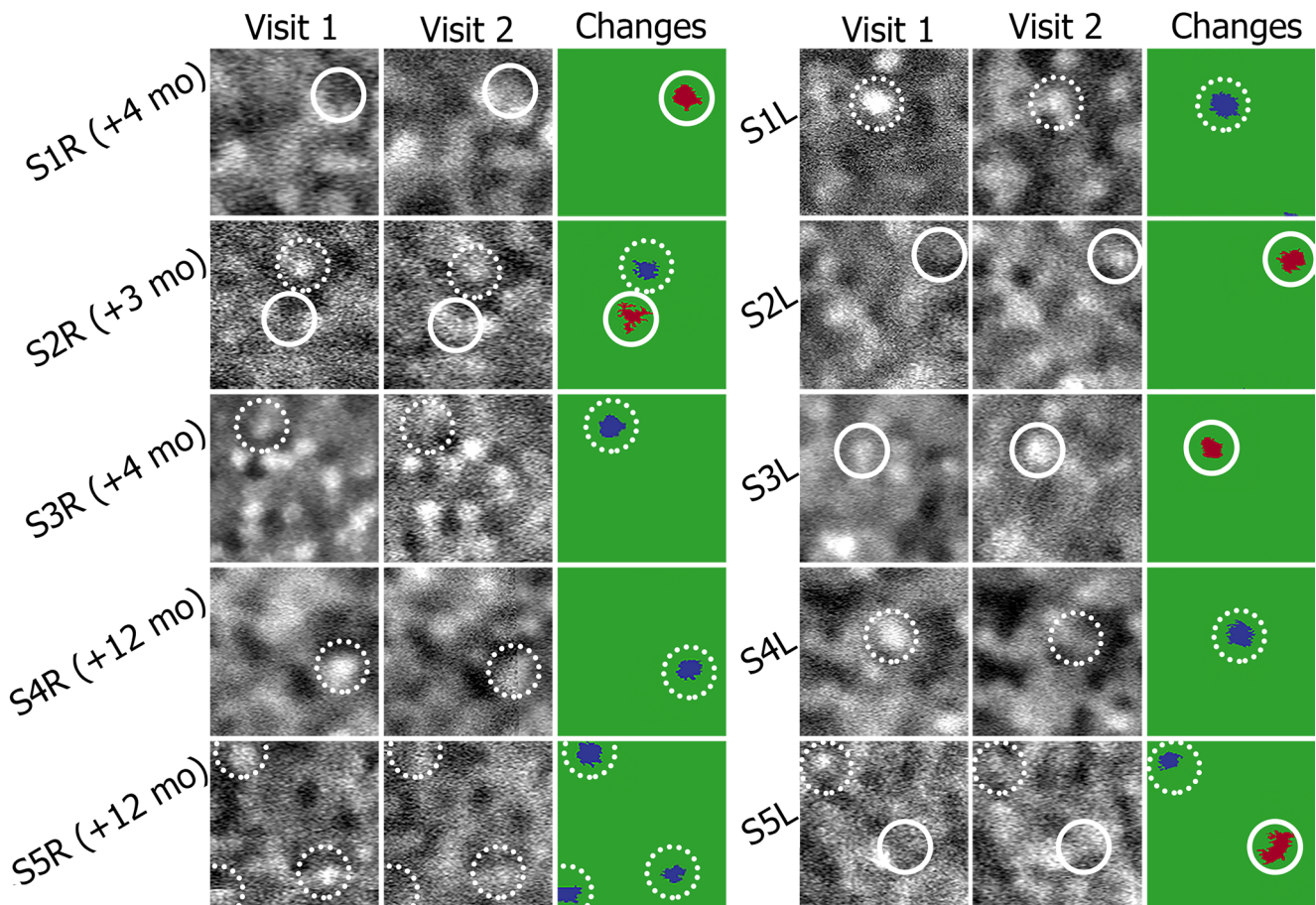
Figure 4. Long-term stability of the fluorescence pattern. Repeatability of AO-ICG signal in 10 eyes from 5 human subjects with a repeated injection (months afterward). All ROIs are 100 μm × 100 μm. Subject codes are shown to the left of each pair, along with the time interval between visits in months. The third column represents automatically detected changes in fluorescence (27) between image pairs, where red (solid circles) denote increases in fluorescence and blue (dotted circles) denote decreases. The overall pattern is conserved across visits for all time points, with over 97% of the areas tested remaining unchanged (16,495 pairs of RPE cells total across 10 eyes).

sured in a coregistered ROI across visits, increased 12.7% from 22.9–25.8 μm, which is slightly larger than the expected repeatability of RPE spacing measurements across visits in healthy subjects (6.5% ± 2.7%, mean ± SD, 6 eyes from 3 subjects; Supplemental Table 4).

These examples illustrate the application of AO-ICG for qualitatively and quantitatively evaluating the status of RPE cells in diseases that affect the outer retina.

Discussion

A major advantage of AO-ICG is that it can be used to longitudinally assess the status of RPE cells directly in the living human eye. In this paper, we show that, following systemic injection of ICG dye, the RPE cells quickly take up circulating dye in a unique but repeatably heterogeneous manner that is maintained over a period of at least 12 months. The observed mosaicism appears to be an intrinsic property of the in vivo RPE tissue (which can be thought of as a fluorescent signature) and cannot be fully explained by the topology of the underlying choriocapillaris vasculature or by the heterogeneous distribution of melanin pigment in the RPE cells. The heterogeneous pattern was most robustly visible following systemic injection, as opposed to following incubation in cell culture, in which we did not observe an obvious heterogeneous pattern (Supplemental Figure 6). In comparison, RPE cells imaged in vivo in patients with OCA showed a clear heterogeneous pattern (Figure 5). All in all, this implies that the overall tissue hierarchy of the choriocapillaris-Bruch's membrane-RPE complex is a critical prerequisite to formation of the fluorescent signature. Given the high degree of mosaicism that naturally exists in the RPE (7), it is not surprising that its response to ICG dye administration also exhibits mosaicism.
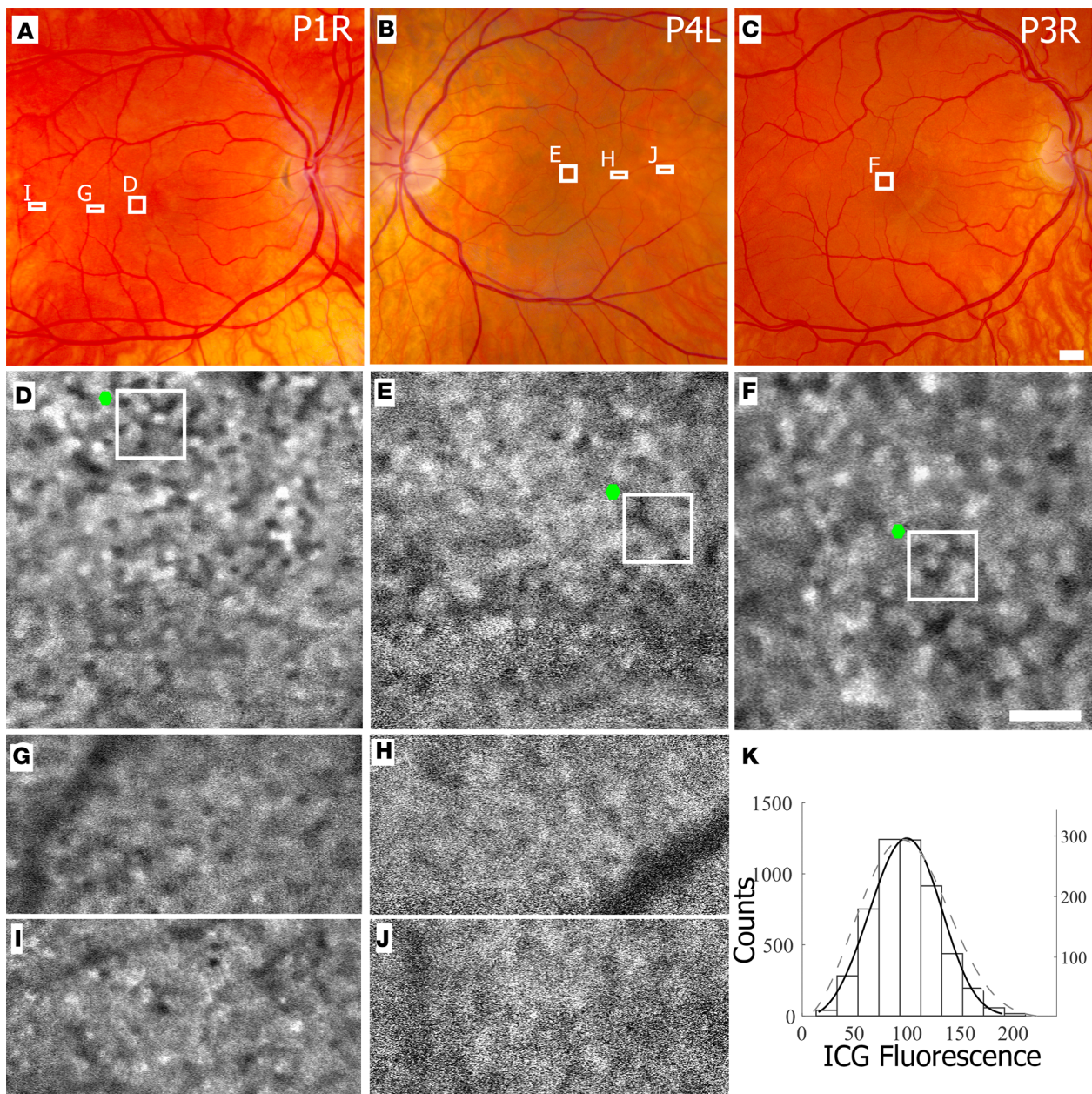
Figure 5. Fluorescence pattern in patients with reduced ocular pigmentation. (**A–C**) Color fundus photo showing areas where AO-ICG images were taken. (**D–J**) The heterogeneous AO-ICG pattern observed in 3 patients with OCA (P1, P4, and P3). AO-ICG images in patients with OCA acquired (**D–F**) near the fovea and at retinal eccentricities of (**G**) 1.7 mm, (**H**) 1.4 mm, (**I**) 3.2 mm, and (**J**) 2.8 mm in the temporal direction. Foveal RPE spacing was significantly increased relative to normal (P1, 19.3 μm; P3, 19.6 μm; P4, 21.5 μm; $P < 0.01$, 2 tailed t test). Small green hexagons indicate the RPE spacing measured from within 100 μm × 100 μm ROIs (white boxes). (**K**) Distribution of ICG fluorescence in RPE cells segmented from patients P1 and P3 (intensity data from P4 was excluded due to poor signal to noise). The distribution was similar to that of pigmented subjects (dashed line) ($P = 0.34$, $n = 5,182$ RPE cells, Kruskal-Wallis one-way ANOVA). Scale bars: (**A–C**) 500 μm, (**D–J**) 100 μm.

Counterintuitively, there is no direct relationship between the health or function of a cell and its fluorescence intensity, with neighboring RPE cells exhibiting strikingly different levels of fluorescence. However, this feature enables neighboring cells to be distinguished from each other, a property that we leveraged to implement algorithms to quantify cell spacing. Furthermore, the fortuitous finding that the heterogeneous pattern can be regenerated with a repeat injection enables quantitative tracking of the pattern across time, revealing stability (Figure 6, E and F) and progression (Figure 6, H and I) in diseases affecting the RPE. In contrast, assessment of RPE using conventional clinical approaches such as fundus autofluorescence are limited in their ability to reveal cellular information. The possibility to detect subclin-

JCI insight
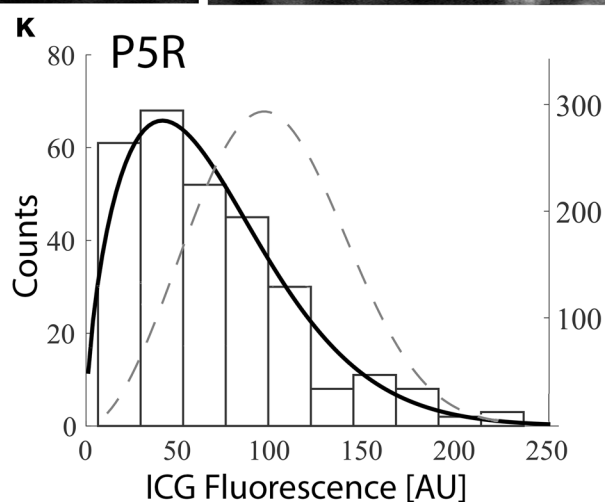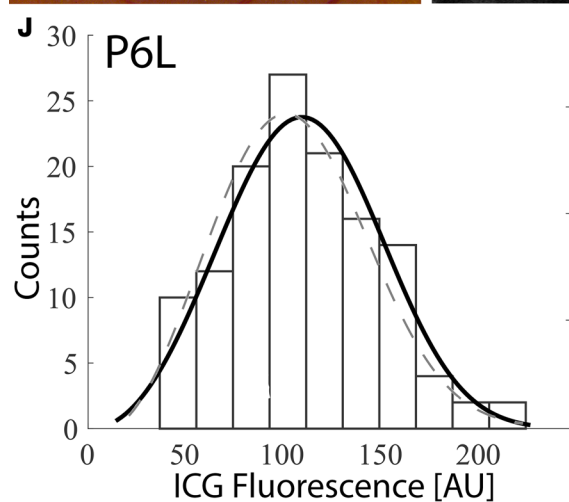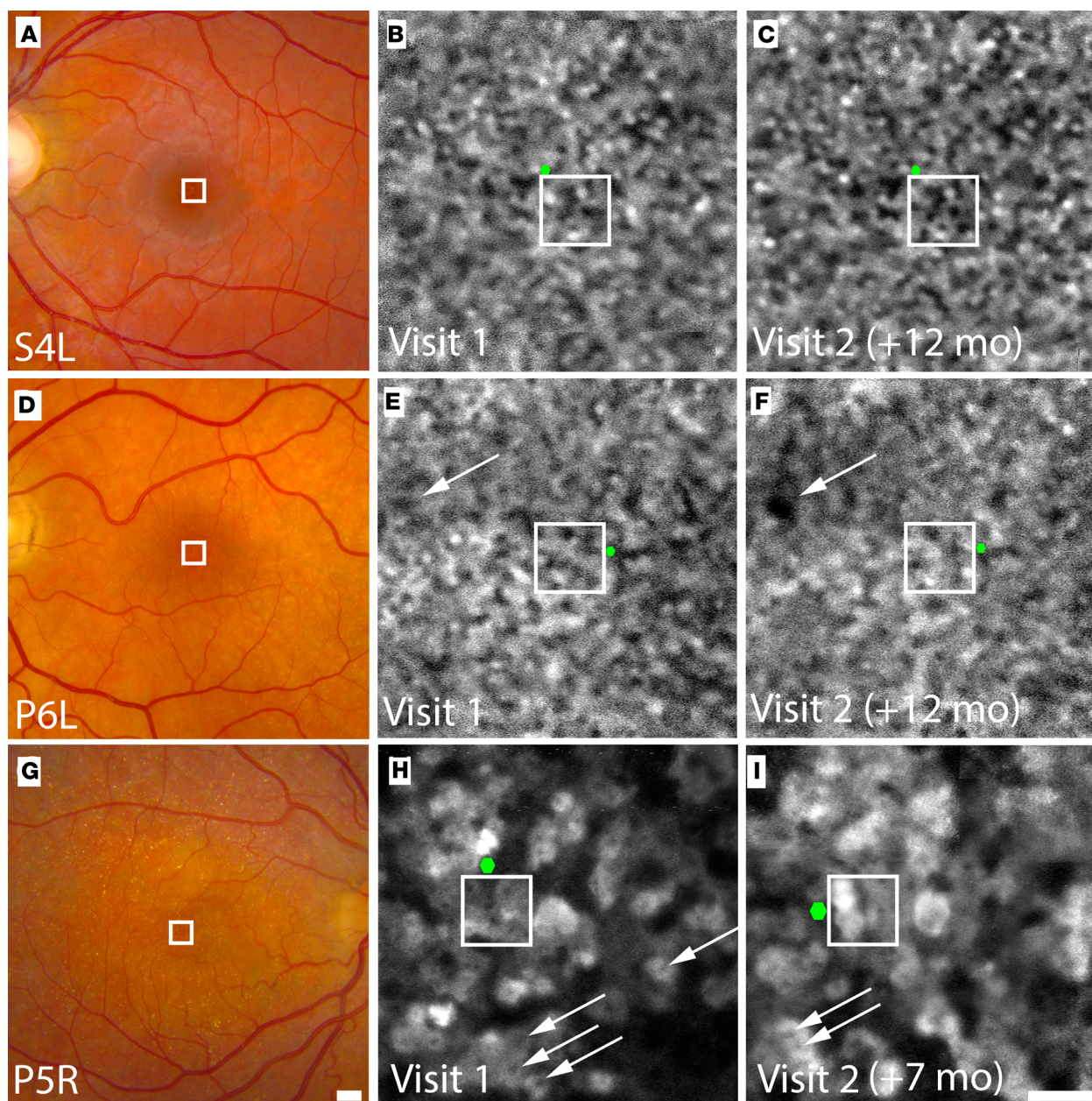
Figure 6. Evaluation of the degree of progressive RPE changes in patients. Clinical applications of AO-ICG in (**A–C**) a healthy eye and in patients with (**D–F**) late-onset retinal degeneration (L-ORD) and (**G–I**) Bietti Crystalline Dystrophy (BCD). (**A**, **D**, and **G**) Color fundus photographs. White boxes indicate a 500 μm × 500 μm ROI in which overlapping AO-ICG images were acquired. Scale bar: 500 μm. (**B**, **C**, **E**, **F**, **H**, and **I**) Longitudinal AO-ICG images of foveal cells acquired in a healthy eye and diseased eyes. AO-ICG images on the second visit were generated with a new injection of ICG. Small green hexagons indicate the RPE spacing measured from within the 100 μm × 100 μm ROIs (white boxes). The RPE mosaic in the patient with L-ORD was similar to that of healthy eyes (98.7% stability across 2 visits; cell spacing z-score, 0.76). There was 1 hypofluorescent spot spanning several cell widths across that appeared in the second visit (arrows in **E** and **F**). In contrast, in the patient with BCD, RPE cells are markedly enlarged (84.5% stability across 2 visits; cell spacing z-score, –8.7), and many RPE nuclei can be visible even in the foveal region (arrows). There are larger RPE cells present outside of the ROI in (**H** and **I**). Scale bar for AO-ICG images: 100 μm. (**J** and **K**) Foveal RPE fluorescence distribution in the patients, averaged across both visits counts indicated on left axis. The overall distributions were significantly different compared with normal, dashed lines (P6L, *n* = 128 RPE cells, *P* < 0.001; P5R, *n* = 288 RPE cells, *P* < 0.001, Kruskal-Wallis one-way ANOVA). Solid line, fit to Weibull distribution. The expected fluorescence distribution from normal data presented in this manuscript is overlaid in the gray dashed lines (counts indicated by axis on right side).

ical changes to the RPE over a period of 7 months (Figure 6, H and I) suggests that quantitative metrics derived from AO-ICG data may be useful as highly sensitive endpoint measures for clinical trials related to restoring or preserving RPE cells.

We introduce a translational imaging framework, in which ICG provided a direct link across images acquired in cells, animals, and humans. Together, the data ultimately result in the improved interpretation of clinical AO-ICG images, allowing us to rapidly translate concepts from the bench to the clinic and back. For example, using the translational imaging framework, we provide the first evidence to our knowledge that the IRAF signal arises from melanin, which had previously been assumed but not shown. This enabled us to explore the relationship between RPE mosaicism and melanin in the living human eye. Second, we confirmed that ICG accumulates in the cytoplasmic space by imaging across cells, mice (2 nuclei of binuclear murine RPE cells clearly visible), and humans (eccentric RPE cells in Supplemental Figure 3 and diseased cells in vivo in Figure 6, H and I), building upon our earlier report of this phenomenon (3). This opens up possibilities for visualizing RPE nuclei in the future, with improved instrumentation leading to higher resolution. We expect that this ICG-based translational imaging framework will be a powerful tool for the in situ, longitudinal, real-time tracking of RPE degenerative diseases.

Our data provide a key insight into how the heterogeneous pattern is formed. In particular, if the pattern were formed simply based upon uptake of dye from the vasculature into the RPE cells, then one would expect that the fluorescence of RPE cells above vessels would be higher than the fluorescence above flow voids, which is the opposite of what our data demonstrate. Moreover, we do not observe strictly monotonic increases in fluorescence (there is a subset of cells that change from hyper to hypofluorescent in Figure 2). This implies that, following the initial uptake stage (first minute) during which clusters of neighboring RPE cells take up similar amounts of ICG dye (exhibiting nearly identical levels of fluorescence), there is a "clearance" stage (second to fifth minute) during which RPE cells that are above choriocapillaris vessel segments appear to clear more dye than those not above vessels. Importantly, the AO-ICG RPE pattern reaches stability before the ICG dye has cleared from the vasculature and remains stable long after the ICG dye has cleared from the vasculature (33), which means that the mosaicism observed in the RPE does not fully depend on the plasma concentration of ICG, which decays rapidly, with a half-life of minutes. In addition, we do not observe an obvious imprinting effect from the underlying vasculature onto the overlying RPE (Supplemental Figure 4). It is important to note that the size scale of the vessel segments and flow voids revealed by AO-ICG are not related to the size of the much larger choriocapillaris lobules, which range in size from about 200–350 μm (37). Altogether, these data corroborate our claim that the heterogeneous AO-ICG pattern is an intrinsic property of the in vivo RPE mosaic, which arises from the in vivo tissue hierarchy and appears to be formed during the initial portion of the "clearance" phase of ICG after the initial uptake.

The main advantage of this technique is that it is nondestructive and provides a way to track tissue heterogeneity over short and long periods of time. AO-ICG does not cause any detectable bleaching of the ICG fluorescence (Supplemental Figure 7 and Supplemental Table 5, *P* = 0.45, 1-tailed paired *t* test); it should be noted that the light levels used here, 135 μW of 790 nm, are less than those reported to cause bleaching (160 μW of 796 nm light; ref. 38), but there could be other factors, as well. Although administration of ICG is not without risks, the risk for adverse reactions is very low (39), and there is potentially information about the status of RPE cells that can only be gleaned from a technique such as AO-ICG. The quantitative metrics that we have developed for evaluating the RPE will be important for use as potential endpoint measures in upcoming clinical trials. Currently, the large majority of AO-based metrics (40) have

limited applicability to the RPE due to the difficulty in reliably imaging the RPE. The measurements of RPE spacing, fluorescence distribution, and longitudinal pattern changes that we introduce in this paper will complement recently developed tools to segment and track the overlying cone photoreceptors (41, 42), which can be simultaneously imaged using multimodal AO imaging (Supplemental Figure 3; refs. 3, 43). We were able to successfully acquire images of the RPE mosaic from patients with various diseases (in addition to a cohort of 23 eyes, the largest in vivo database of RPE spacing to date, to our knowledge), a feat that has historically been challenging. In our multimodal AO instrument, simultaneously captured coregistered darkfield (24) and AO-IRAF (5) images were not successful at revealing the entire RPE mosaic; this illustrates the robustness of the AO-ICG signal for imaging patients. This robustness is supported by our overall success (75%) in imaging RPE cells in the 4 patients with nystagmus, among the most challenging of patient populations to image using AO.

All in all, AO-ICG opens up exciting opportunities to evaluate the status and progression of disease. We expect that the combination of imaging cells, animals, and patients using ICG will form a powerful tool for revealing the pathophysiology of diseases and for accelerating clinical trials.

Methods

Clinical evaluation of human subjects. Fourteen healthy subjects with visual acuity of 20/20 or better, no history or signs of ocular disease in at least 1 eye, and no known allergies to shellfish, iodine, or ICG were recruited for this study (NCT02317328; https://clinicaltrials.gov). Participants who were willing to return for additional visits were invited for additional imaging, consisting of either follow-up AO imaging alone (days afterward), repeated AO with ICG injection on a subsequent visit 3–12 months later, or both. Additionally, 4 patients with OCA (single visit), 1 patient with L-ORD (2 visits spaced 12 months apart), and 1 patient with BCD (2 visits 7 months apart) were included in this study. All patients underwent best corrected visual acuity testing, dilated funduscopic examination, color fundus (Topcon) and autofluorescence imaging (Spectralis, Heidelberg Engineering. All patients underwent genetic testing prior to recruitment for this study and had molecularly confirmed diagnoses. Patients were recruited from the National Eye Institute eye clinic.

Clinical AO imaging. Eyes were dilated with 2.5% phenylephrine hydrochloride (Akorn Inc) and 1% tropicamide (Sandoz, A Novartis Division). A custom-assembled multimodal AO retinal imager based on previously described designs (3, 5), outfitted with a computer-controlled fixation system (44), was used to acquire images before, during (from injection to approximately 10 minutes after injection), and after (starting from approximately 45 minutes after injection) i.v. administration of ICG at a dose of 25 mg in 3 ml, according to the standard of care at the National Eye Institute Eye Clinic. The approximate lateral resolution of the instrument was 2–3 μm (dependent upon the ocular biometry of each subject, and assuming a beam diameter of 7.75 mm). The imaging field of view varied from approximately 0.23–0.60 mm on the retina, depending on the fixational stability of each subject (smaller fields of view required better fixation) and on the time available to image each subject (smaller fields of view provided better pixel sampling but required more time to cover the same retinal region). The fovea and parafoveal regions were imaged for all subjects, along with images taken along the temporal direction in some subjects to explore the appearance of the AO-ICG signal at eccentric locations. In 1 subject, more extensive imaging was performed at eccentric locations to explore the visibility of nuclei within RPE cells. Videos were recorded at an acquisition rate of approximately 16.7 Hz. Timestamps during video acquisitions were automatically recorded. The acquisition time of each video varied from approximately 9–120 seconds; in general, the shorter acquisition times were used for the latest versions of the instrumentation, described below, due to improved sensitivity. The total image acquisition time for each eye varied between approximately 1 and 3 hours (including short 10–20 second breaks given every few minutes but not including extended breaks given every 30–60 minutes), depending on the imaging protocol (Supplemental Table 1). Approximately 9–85 overlapping locations were imaged per eye. For longitudinal imaging, imaging data from the previous visit was used as a reference to ensure that the same retinal regions were being covered.

AO instrumentation. Subjects were imaged using either the initial versions of the instrumentation based on an 850-nm wavefront–sensing light source and an 830 nm dichroic beamsplitter to effectively collect light between 810 and 830 nm (3, 5) or an improved version using an 880-nm wavefront–sensing light source (Superlum SLD-mCS-341-HP1-SM-880) with 900/32 clean-up filters placed in front of the light source and wavefront sensor (Semrock FF01-900/32) and a custom 855-nm dichroic beamsplitter to effectively collect light between 810–850 nm (Semrock). In addition to AO-ICG (3), confocal reflectance (45),

and split detection (46) images were simultaneously acquired. AO-IRAF (5) was acquired prior to AO-ICG imaging since they share the same detection channel and simultaneous acquisition is not possible. The other simultaneously acquired channels were used to coregister AO-IRAF and AO-ICG images to each other. The power of the light measured at the cornea was fixed for each imaging session but varied from day to day due to instrument alignment. Measured light powers, taken at the beginning of each imaging day, were less than 135 µW for the 790-nm light source, 35 µW for the 850-nm light source, and 40 µW for the 880-nm light source. These were below the maximum permissible exposure limits set by the American National Standards Institute standard Z136.1 2014 (either the 850 nm or the 880 nm light source was used but not both simultaneously; ref. 34).

AO image analysis. Eye motion was corrected after image acquisition (47) using one of the simultaneously acquired channels (3). Averaged AO images were assembled into montages of overlapping retinal regions; then, ROIs were selected and scaled for analysis, as previously described (48). Longitudinal imaging datasets were registered within visits and then manually overlaid on top of each other based on vascular features and other landmarks. Pairs of larger ROIs (500 µm × 500 µm) were used to quantify changes between visits based on a previously validated algorithm that employs pictorial structures and tree-based belief propagation to track patterns across visits; patterns were represented as superpixels (Figure 1B and Supplemental Figure 3), which were also used to assist with cell identification (27). Smaller ROIs (100 µm × 100 µm) within 0.20 mm of the fovea (subjectively identified based on the cone packing arrangement as previously described; ref. 48) were selected for quantification of cell-to-cell spacing (49) based on the density recovery profile (50, 51). Videos acquired during the first 10 minutes after injection were coregistered to each other by selecting a single reference frame from 1 of the videos in the sequence and then registering all videos to the same reference frame. Frames that could not be reliably registered to the reference frame were discarded, and timestamp data were used to determine the timing of each successfully registered frame. For the analysis comparing AO-ICG fluorescence intensity with the underlying choriocapillaris pattern, images of the choriocapillaris were generated using the transit phase of ICG, as previously described (30). The choriocapillaris images were enhanced using a high-pass filter (radius ~23 µm, using Photoshop, Adobe) to minimize the presence of larger choroidal vessels, were histogram stretched to enhance the visibility of flow voids, and were segmented using the Frangi vesselness filter (52). Images of choriocapillaris and RPE were coregistered using simultaneously acquired confocal reflectance images for categorization of pixels into those overlying vessels and those overlying flow voids. To assess whether AO-ICG resulted in bleaching of the ICG signal, conventional ICG images were acquired in a total of 7 eyes (Spectralis HRA+OCT, Heidelberg Engineering) immediately after AO-ICG imaging was completed. Following coregistration of overlapping AO-ICG images onto conventional ICG images, for each eye, 6 ROIs (450 µm × 450 µm; 1 ROI at an area where AO images were taken, and 5 ROIs at areas where no AO images were taken) were selected at eccentricities of 1.5 and 3.0 mm (except for 1 subject, at which eccentricities of 2.4 and 3.9 mm were selected to avoid retinal vessels). The mean ICG fluorescence was computed within each ROI for comparison.

Confocal microscopy of cells. Confluent monolayers of primary human fetal RPE cells were generated from cadaver tissue as described previously (53, 54). iPSC-derived RPE cells were generated from a healthy pigmented human subject and individuals with OCA, as described previously (55, 56). Cells were tested and were negative of mycoplasma. For live cell imaging and detection of IRAF from melanin, RPE cells were seeded on vitronectin-coated cover glass coverslip bottom multiwell chamber slides (Thermo Fisher Scientific) and cultured for 6–8 weeks, until they formed a confluent monolayer exhibiting typical polygonal RPE morphology. Fetal and/or iPSC-derived pigmented RPE cells were incubated with 20 µM ICG dissolved in cell culture medium for 4 hours (2 hours for the albinism patient–derived RPE) and were then washed twice with the culture media at fixed time points prior to microscopy (OCA iPSC-RPE) or immediately prior to microscopy (fetal and pigmented iPSC-RPE cells). A custom-modified confocal microscope (SP8, Leica) equipped with 690 and 730 nm CW laser diodes was used for ICG and IRAF imaging, respectively. Due to the long emission wavelengths needed for ICG and IRAF, avalanche photodiodes (APDs) with an 810/90 nm bandpass filter were used for signal detection. Transmitted light images were captured either simultaneously or sequentially using a 488 nm CW laser diode and a transmitted light photomultiplier tube (PMT-trans) detector. Images were acquired using a 20×/0.75 numerical aperture (NA) (OCA iPSC-RPE) or a 40×/1.30 NA and/ or 63×/1.40 NA objective (fetal and pigmented iPSC-RPE cells). All cell imaging was performed live while maintaining 5% CO_2 and 37°C conditions.

Translational AO imaging in mice. All mice were housed in the NIH animal facilities. Female albino mice (BALB/cJ, stock 000651, The Jackson Laboratory) aged 4 months were i.p. injected with 200 µl of 5 mg/ml ICG (3) (or left uninjected) approximately 16 hours before ex vivo microscopy. Immediately prior to and after ICG administration, mouse eyes were imaged using a scanning laser ophthalmoscope (Heidelberg Spectralis) to verify absence and delivery of ICG to the eye. On the day of microscopy, mice were euthanized by CO_2 inhalation, and then 1 eye was enucleated. The anterior segment was dissected at the limbus with Vannas spring scissors 15000-08 (Fine Science Tools) and Dumont #5 Fine Forceps (Fine Science Tools). The lens was removed from the vitreous cavity. The neural retina was gently detached from the RPE with fine forceps and separated from the eye cup by cutting the optic nerve head. The eye cup was transferred to a clean glass slide. A scalpel was used to produce 4–5 radial cuts at the margins of the eye cup, allowing the preparation to flatten. Fresh, unfixed tissues were mounted using Immu-Mount (Thermo Fisher Scientific) and then immediately imaged on the translational AO imager.

The custom-assembled AO instrument described above was modified into an inverted microscope by adding a fold mirror to send light vertically upward, followed by an achromatic doublet (focal length = 19 mm, 12.7-mm diameter; AC127-019-B-ML, Thorlabs) conjugate to the pupil plane of the instrument, which served as the objective of the microscope (NA comparable with that of the human eye). Immediately prior to image acquisition, a piece of paper was placed at the focal plane of the objective and a static AO correction was applied immediately before the sample was introduced. Images were acquired as described under clinical AO imaging at either 16.7 or 30 Hz.

Statistics. All data are presented as mean ± SD. Distributions of fluorescence histograms were compared with Kruskal-Wallis one-way ANOVA. One-way ANOVA was used to compare the RPE spacing measurements between contralateral eyes in healthy eyes and comparison between AO-IRAF and AO-ICG fluorescence values in 2 healthy subjects. Two-tailed paired Student's t tests were used for comparing ICG fluorescence in RPE cells above the vessels compared with above flow voids of choriocapillaris and comparing RPE spacing of patients vs. healthy subjects. Z-scores were calculated to assess longitudinal changes for coregistered patches of retina. One-tailed paired t test was used to determine whether AO-ICG resulted in bleaching (reduction of) the ICG fluorescence signal. In all test statistics, $P < 0.05$ was considered significant.

Study approval. For cells, iPSC-RPE generation from human subjects was approved by the IRB of the NIH (NCT01432847). Cadaver tissue (fetal RPE cells) is exempt from IRB review. For animals, experiments were conducted according to protocols approved by the NIH IACUC. For human subjects, the study was approved by the IRB of the NIH (NCT02317328). Research procedures adhere to the tenets of the Declaration of Helsinki. Written, informed consent was obtained from all participants after the nature of the research and possible consequences of the study were explained.

Author contributions

JT conceived and designed the experiments. HJ, JL, TL, AG, MGS, SC, RF, and JT performed the experiments. HJ, JL, TL, and JT analyzed the data. AG, MGS, SC, RS, OS, AM, KB, RF, and JT contributed reagents/materials. CC, LAH, and BPB contributed patient referrals. JT wrote the paper. All authors reviewed and edited the paper.

Acknowledgments

HaeWon Jung's present address is Indiana University, Bloomington, Indiana, USA.

Address correspondence to: Johnny Tam, Ophthalmic Genetics and Visual Function Branch, 10 Center Drive Room 10N109, MSC1860, Bethesda, Maryland 20892, USA. Phone: 301.435.7821; Email: johnny@nih.gov.

1. Wang D, Bodovitz S. Single cell analysis: the new frontier in 'omics'. *Trends Biotechnol*. 2010;28(6):281–290.
2. Galler K, Bräutigam K, Große C, Popp J, Neugebauer U. Making a big thing of a small cell--recent advances in single cell analysis. *Analyst*. 2014;139(6):1237–1273.
3. Tam J, Liu J, Dubra A, Fariss R. In Vivo Imaging of the Human Retinal Pigment Epithelial Mosaic Using Adaptive Optics Enhanced Indocyanine Green Ophthalmoscopy. *Invest Ophthalmol Vis Sci*. 2016;57(10):4376–4384.
4. Strauss O. The retinal pigment epithelium in visual function. *Physiol Rev*. 2005;85(3):845–881.
5. Liu T, Jung H, Liu J, Droettboom M, Tam J. Noninvasive near infrared autofluorescence imaging of retinal pigment epithelial cells in the human retina using adaptive optics. *Biomed Opt Express*. 2017;8(10):4348–4360.
6. Weiter JJ, Delori FC, Wing GL, Fitch KA. Retinal pigment epithelial lipofuscin and melanin and choroidal melanin in human eyes. *Invest Ophthalmol Vis Sci*. 1986;27(2):145–152.
7. Burke JM, Hjelmeland LM. Mosaicism of the retinal pigment epithelium: seeing the small picture. *Mol Interv*. 2005;5(4):241–249.
8. Milenkovic A, et al. Bestrophin 1 is indispensable for volume regulation in human retinal pigment epithelium cells. *Proc Natl Acad Sci USA*. 2015;112(20):E2630–E2639.
9. MacDonald IM, Lee T. Best Vitelliform Macular Dystrophy. In Adam MP, et al, eds. *GeneReviews*. Seattle, Washington: University of Washington; National Center for Biotechnology Information Web site. https://www.ncbi.nlm.nih.gov/books/NBK1167/. Updated December 13, 2013. Accessed February 20, 2019.
10. Bietti G. Ueber familiares Vorkommen von "Retinitis punkutata albescens" (verbunden mit "Dystrophia marginalis cristallinea corneae"), Glitzern des Glaskorpers und anderen degenerativen Augenveranderungen. *Klin Monatsbl Augenheilkd*. 1937;99:737–756.
11. Li A, et al. Bietti crystalline corneoretinal dystrophy is caused by mutations in the novel gene CYP4V2. *Am J Hum Genet*. 2004;74(5):817–826.
12. Moiseyev G, Chen Y, Takahashi Y, Wu BX, Ma JX. RPE65 is the isomerohydrolase in the retinoid visual cycle. *Proc Natl Acad Sci USA*. 2005;102(35):12413–12418.
13. Redmond TM. RPE65 takes on another role in the vertebrate retina. *Proc Natl Acad Sci USA*. 2017;114(41):10818–10820.
14. Hayward C, et al. Mutation in a short-chain collagen gene, CTRP5, results in extracellular deposit formation in late-onset retinal degeneration: a genetic model for age-related macular degeneration. *Hum Mol Genet*. 2003;12(20):2657–2667.
15. Ayyagari R, et al. Late-onset macular degeneration and long anterior lens zonules result from a CTRP5 gene mutation. *Invest Ophthalmol Vis Sci*. 2005;46(9):3363–3371.
16. Cukras C, Flamendorf J, Wong WT, Ayyagari R, Cunningham D, Sieving PA. LONGITUDINAL STRUCTURAL CHANGES IN LATE-ONSET RETINAL DEGENERATION. *Retina (Philadelphia, Pa)*. 2016;36(12):2348–2356.
17. Jager RD, Mieler WF, Miller JW. Age-related macular degeneration. *N Engl J Med*. 2008;358(24):2606–2617.
18. Bhutto I, Lutty G. Understanding age-related macular degeneration (AMD): relationships between the photoreceptor/retinal pigment epithelium/Bruch's membrane/choriocapillaris complex. *Mol Aspects Med*. 2012;33(4):295–317.
19. Keilhauer CN, Delori FC. Near-infrared autofluorescence imaging of the fundus: visualization of ocular melanin. *Invest Ophthalmol Vis Sci*. 2006;47(8):3556–3564.
20. Holz F, Spaide R, Bird AC, Schmitz-Valckenberg S (eds). Origin of Fundus Autofluorscence. In: *Atlas of Fundus Autofluorscence Imaging*. Berlin, Heidelberg, Germany: Springer Berlin Heidelberg; 2007:17–29.
21. Liang J, Williams DR, Miller DT. Supernormal vision and high-resolution retinal imaging through adaptive optics. *J Opt Soc Am A Opt Image Sci Vis*. 1997;14(11):2884–2892.
22. Morgan JI, Dubra A, Wolfe R, Merigan WH, Williams DR. In vivo autofluorescence imaging of the human and macaque retinal pigment epithelial cell mosaic. *Invest Ophthalmol Vis Sci*. 2009;50(3):1350–1359.
23. Roorda A, Zhang Y, Duncan JL. High-resolution in vivo imaging of the RPE mosaic in eyes with retinal disease. *Invest Ophthalmol Vis Sci*. 2007;48(5):2297–2303.
24. Scoles D, Sulai YN, Dubra A. In vivo dark-field imaging of the retinal pigment epithelium cell mosaic. *Biomed Opt Express*. 2013;4(9):1710–1723.
25. Liu Z, Kocaoglu OP, Miller DT. 3D Imaging of Retinal Pigment Epithelial Cells in the Living Human Retina. *Invest Ophthalmol Vis Sci*. 2016;57(9):OCT533–OCT543.
26. Liu T, Jung H, Liu J, Droettboom M, Tam J. Noninvasive near infrared autofluorescence imaging of retinal pigment epithelial cells in the human retina using adaptive optics. *Biomed Opt Express*. 2017;8(10):4348–4360.
27. Liu J, Jung H, Tam J. COMPUTER-AIDED DETECTION OF PATTERN CHANGES IN LONGITUDINAL ADAPTIVE OPTICS IMAGES OF THE RETINAL PIGMENT EPITHELIUM. *Proc IEEE Int Symp Biomed Imaging*. 2018;2018:34–38.
28. Roorda A, Williams DR. Optical fiber properties of individual human cones. *J Vis*. 2002;2(5):404–412.
29. Zhang P, Goswami M, Zawadzki RJ, Pugh EN. The Photosensitivity of Rhodopsin Bleaching and Light-Induced Increases of Fundus Reflectance in Mice Measured In Vivo With Scanning Laser Ophthalmoscopy. *Invest Ophthalmol Vis Sci*. 2016;57(8):3650–3664.
30. Jung H, Liu T, Liu J, Huryn LA, Tam J. Combining multimodal adaptive optics imaging and angiography improves visualization of human eyes with cellular-level resolution. *Commun Biol*. 2018;1:189.
31. Mori K, Gehlbach PL, Nishiyama Y, Deguchi T, Yoneya S. The ultra-late phase of indocyanine green angiography for healthy subjects and patients with age-related macular degeneration. *Retina (Philadelphia, Pa)*. 2002;22(3):309–316.
32. Zonios G, Dimou A, Bassukas I, Galaris D, Tsolakidis A, Kaxiras E. Melanin absorption spectroscopy: new method for non-invasive skin investigation and melanoma detection. *J Biomed Opt*. 2008;13(1):014017.
33. Desmettre T, Devoisselle JM, Mordon S. Fluorescence properties and metabolic features of indocyanine green (ICG) as related to angiography. *Surv Ophthalmol*. 2000;45(1):15–27.
34. ANSI Z136.1 - 2014. American National Standard for Safe Use of Lasers, Laser Institute of America web site. https://www.lia.org/store/product/ansi-z1361-2014-safe-use-lasers-electronic-version. Accessed February 20, 2019.
35. Wilk MA, et al. Relationship between foveal cone specialization and pit morphology in albinism. *Invest Ophthalmol Vis Sci*. 2014;55(7):4186–4198.
36. Hata M, et al. Reduction of lipid accumulation rescues Bietti's crystalline dystrophy phenotypes. *Proc Natl Acad Sci USA*. 2018;115(15):3936–3941.

37. Olver JM. Functional anatomy of the choroidal circulation: methyl methacrylate casting of human choroid. *Eye (Lond)*. 1990;4(Pt 2):262–272.

38. Granger CE, et al. Human Retinal Pigment Epithelium: In Vivo Cell Morphometry, Multispectral Autofluorescence, and Relationship to Cone Mosaic. *Invest Ophthalmol Vis Sci*. 2018;59(15):5705–5716.

39. Garski TR, Staller BJ, Hepner G, Banka VS, Finney RA. Adverse reactions after administration of indocyanine green. *JAMA*. 1978;240(7):635.

40. Tam J. Adaptive Optics and Its Use in Inflammatory Eye Disease. In: Sen HN, Read RW, eds. *Multimodal Imaging in Uveitis*. Cham, Switzerland: Springer International Publishing; 2018:135–149.

41. Liu J, Jung H, Tam J. Accurate Correspondence of Cone Photoreceptor Neurons in the Human Eye Using Graph Matching Applied to Longitudinal Adaptive Optics Images. *Med Image Comput Comput Assist Interv*. 2017;10434:153–161.

42. Liu J, Jung H, Dubra A, Tam J. Cone Photoreceptor Cell Segmentation and Diameter Measurement on Adaptive Optics Images Using Circularly Constrained Active Contour Model. *Invest Ophthalmol Vis Sci*. 2018;59(11):4639–4652.

43. Liu Z, Tam J, Saeedi O, Hammer DX. Trans-retinal cellular imaging with multimodal adaptive optics. *Biomed Opt Express*. 2018;9(9):4246–4262.

44. Rossi EA, et al. In vivo imaging of retinal pigment epithelium cells in age related macular degeneration. *Biomed Opt Express*. 2013;4(11):2527–2539.

45. Dubra A, Sulai Y. Reflective afocal broadband adaptive optics scanning ophthalmoscope. *Biomed Opt Express*. 2011;2(6):1757–1768.

46. Scoles D, et al. In vivo imaging of human cone photoreceptor inner segments. *Invest Ophthalmol Vis Sci*. 2014;55(7):4244–4251.

47. Dubra A, Harvey Z. Registration of 2D Images from Fast Scanning Ophthalmic Instruments. In: Fischer B, Dawant BM, Lorenz C, eds. *Biomedical Image Registration*. Berlin, Heidelberg, Germany: Springer; 2010:60–71.

48. Liu J, Jung H, Dubra A, Tam J. Automated Photoreceptor Cell Identification on Nonconfocal Adaptive Optics Images Using Multiscale Circular Voting. *Invest Ophthalmol Vis Sci*. 2017;58(11):4477–4489.

49. Cooper RF, Wilk MA, Tarima S, Carroll J. Evaluating Descriptive Metrics of the Human Cone Mosaic. *Invest Ophthalmol Vis Sci*. 2016;57(7):2992–3001.

50. Duncan JL, et al. High-resolution imaging with adaptive optics in patients with inherited retinal degeneration. *Invest Ophthalmol Vis Sci*. 2007;48(7):3283–3291.

51. Rodieck RW. The density recovery profile: a method for the analysis of points in the plane applicable to retinal studies. *Vis Neurosci*. 1991;6(2):95–111.

52. Frangi AF, Niessen WJ, Vincken KL, Viergever MA. Multiscale vessel enhancement filtering. In Wells WM, Colchester A, Delp S, eds. *Medical Image Computing and Computer-Assisted Intervention — MICCAI'98*. Berlin, Heidelberg, Germany:Springer-Verlag; 1998:130–137.

53. Maminishkis A, et al. Confluent monolayers of cultured human fetal retinal pigment epithelium exhibit morphology and physiology of native tissue. *Invest Ophthalmol Vis Sci*. 2006;47(8):3612–3624.

54. Maminishkis A, Miller SS. Experimental Models for Study of Retinal Pigment Epithelial Physiology and Pathophysiology. *J Vis Exp*. 2010;(45):e2032–e2032.

55. Miyagishima KJ, et al. In Pursuit of Authenticity: Induced Pluripotent Stem Cell-Derived Retinal Pigment Epithelium for Clinical Applications. *Stem Cells Transl Med*. 2016;5(11):1562–1574.

56. May-Simera HL, et al. Primary Cilium-Mediated Retinal Pigment Epithelium Maturation Is Disrupted in Ciliopathy Patient Cells. *Cell Rep*. 2018;22(1):189–205.